JET PRODUCTION IN HIGH-ENERGY HADRON-PROTON COLLISIONS*

C. BROMBERG[1], G. FOX, R. GOMEZ, J. PINE, J. ROHLF, S. STAMPKE and K. YUNG

California Institute of Technology, Pasadena, California 91125, USA

S. ERHAN, E. LORENZ[2], M. MEDINNIS and P. SCHLEIN

University of California, Los Angeles, California 90024, USA

V. ASHFORD[3], H. HAGGERTY, R. JUHALA[4], E. MALAMUD and S. MORI

Fermi National Accelerator Laboratory, Batavia, Illinois 60510, USA

R. ABRAMS, R. DELZENERO, H. GOLDBERG, S. MARGULIES, D. McLEOD,
J. SOLOMON and R. STANEK

University of Illinois at Chicago Circle, Chicago, Illinois 60680, USA

A. DZIERBA and W. KROPAC[5]

Indiana University, Bloomington, Indiana 47401, USA

We present experimental details from a study of hadron jet production at high transverse momentum ($p_\perp$) in 130 and 200 GeV hadron-proton collisions. Jet definition and acceptance of the apparatus are discussed thoroughly. Jet cross sections are measured for p, π^-, π^+, K^-, K^+, and $\bar{p}$ incident on a liquid hydrogen target. These cross sections depend strongly on the number of valence quarks in the beam. The $p_\perp$ dependence of the jet cross section is measured to be significantly flatter than that for single particles. We show that a model based on quantum chromodynamics (QCD) is able to qualitatively explain both the large jet cross section and the event structure on the trigger and away sides. We present evidence for scale breaking; higher transverse momentum jets are seen to be composed of a greater number of lower momentum particles. The average momentum ($\langle k_\perp \rangle$) of these particles transverse to the jet direction is observed to increase with increasing jet $p_\perp$. Charged particle correlations on both the trigger and away sides are given for both pion and proton beams.

[1] Presently at Michigan State University, East Lansing, Michigan.
[2] Permanently at Max Planck Institute für Physik and Astrophysik, Munich, Germany.
[3] Presently at Brookhaven National Laboratory, Upton, L.I., New York.
[4] Presently at McDonald Douglas Corporation, St. Louis, Missouri.
[5] Presently at Hughes Aircraft Corporation, Los Angeles, California.

1. Introduction

Jet-like structure in hadronic interactions was first observed at the CERN intersecting storage rings in events triggered by single high-$p_\perp$ neutral pions [1]. Since then, we have triggered directly on jets of particles of high collective transverse momentum [2]. Jets are of substantial current interest because the possibility exists that they arise in hadron-hadron collisions from the hard scattering and subsequent fragmentation of constituent partons. We present experimental details of jet studies from the main run of E260 at the Fermilab multi-particle spectrometer (MPS) [3]. Recent results from this experiment have been summarized in ref. [4]. A plan view of the experimental set-up is shown in fig. 1. We triggered on both single particles and jets of particles of high transverse momentum entering either one of two calorimeters. These calorimeters were oriented at a laboratory angle of 100 mrad with respect to the beam axis, which corresponds to roughly 90° in the c.m.s. Details of the apparatus and triggers are given in sects. 2, 3. The track reconstruction and neutral particle fitting are discussed in sect. 4.

The jet events are sufficiently complex that a model is needed in order to calculate geometrical acceptances and trigger biases [1, 5–6]. This has led us to make use of the QCD approach of Feynman, Field, and Fox [7] to model the events as

$$(\text{beam}) + \text{p} \rightarrow 4 \text{ jets} .$$

This event simulation is detailed in sect. 5. Event structure on trigger and away sides is discussed in sect. 6. In sect. 7 we present jet cross sections for various beam types. Comparison is made with theory and previous experiments.

2. Apparatus

2.1. BEAM AND TARGET

Experiment 260 was run in the M6W beam line at Fermilab. Data were taken with an incident beam momentum of 200 GeV/c for both positively and negatively charged particles*. The average beam intensity was about 3×10^6 particles per 1.75 second spill. The beam was focused to a roughly uniform 1.5 cm diameter spot size at our experimental target. The effective (dead-time corrected) beam totals were 6.5×10^{10} positives and 5.9×10^{10} negatives. In addition, a smaller sample of 5.8×10^9 total effective beam was taken at 130 GeV/c.

The incident hadrons were tagged with four Čerenkov counters which we label as C_1, C_2, C_3, and C_4. Counters C_1 and C_2 were threshold counters which were both set to count pions only. C_3 and C_4 were differential counters which were set to

---

* About one-third of this 200 GeV/c running was actually at a beam momentum of 190 GeV/c. We note no difference in the two data samples and combine them without further comment.

PLAN VIEW MULTIPARTICLE SPECTROMETER

SPARK CHAMBER
PROPORTIONAL CHAMBER

BB BB
□   □   y,u,x
w,v

TARGET
(SEE NEXT FIGURE
FOR MORE DETAIL)

CALORIMETER
|E| ELECTRON MODULES
H HADRON MODULES

A
x y u
x' y' v

B'   B C
x y u x y
x' y' v x y

MAGNET YOKE

D
u v x y

MAGNET YOKE

$E_1 E_2 E_3 E_4$
(EACH x,y,u)

22 CELLS
CHERENKOV
COUNTER (CI)

DIAPHRAGMS

2 MIRRORS
(TOP & BOTTOM)

F_{1-4}
(EACH x,y,u)

$F'_L(X)$
LEFT
CALORIMETER

E H
E H
E H
E H

2×2

$F'_{CENTER}(X)$

E H
E H
E H
E H

$F'_R(X)$
RIGHT
CALORIMETER

z meters
x meters

2   1   0   -1   -2

-2   0   2   4   6   8   10   12   14   15

Fig. 1. Plan view of E260 spectrometer.

count protons and kaons, respectively. We defined the 4×3 matrix α_{ij} to be the probability that a particle of type j (pion, kaon, or proton) would fire Čerenkov counter C_i. Using the recorded signal patterns in the sample of recorded events, and the cumulative Čerenkov scalers of the incident beam as input data, we performed a fit for α_{ij} and the beam composition. These fits had two degrees of freedom. The results of the fits are shown in tables 1 and 2. The beam compositions from the fits agree with independent measurements [8]. Pions were selected in the offline analysis as $(C_1 + C_2) \cdot \overline{C}_3 \cdot \overline{C}_4$, kaons as $\overline{C}_1 \cdot \overline{C}_2 \cdot C_3 \cdot \overline{C}_4$, and protons as $\overline{C}_1 \cdot \overline{C}_2 \cdot \overline{C}_3 \cdot C_4$. With these definitions for particle identification, the contaminations in the π^-, K^-, and $\bar{p}$ samples were 0.1%, 0.6%, and 3.3%, respectively. The contaminations in the p, π^+, and K^+ samples were $<0.1\%$, 1.3%, and 1.7%, respectively.

TABLE 1

Results of negative beam fit

	α matrix		
	π^-	K^-	$\bar{p}$
C1	0.692 ± 0.0015	0.052 ± 0.003	0.023 ± 0.002
C2	0.665 ± 0.0015	0.018 ± 0.002	0.000 ± 0.0007
C3	0.000 ± 0.00004	0.011 ± 0.002	0.908 ± 0.017
C4	0.001 ± 0.0001	0.439 ± 0.008	0.000 ± 0.002
Beam composition for triggered events	0.953 ± 0.002 π^- 0.034 ± 0.0005 K^- 0.013 ± 0.0002 $\bar{p}$		
Beam composition	0.953 ± 0.002 π^- 0.0392 ± 0.0005 K^- 0.0075 ± 0.0001 $\bar{p}$		

TABLE 2

Results of positive beam fit

	α matrix		
	π^+	K^+	p
C1	0.676 ± 0.005	0.014 ± 0.006	0.006 ± 0.0002
C2	0.699 ± 0.005	0.085 ± 0.009	0.001 ± 0.0001
C3	0.008 ± 0.0009	0.000 ± 0.006	0.883 ± 0.003
C4	0.008 ± 0.0006	0.517 ± 0.015	0.001 ± 0.0005
Beam composition for triggered events	0.121 ± 0.001 π^+ 0.018 ± 0.0005 K^+ 0.861 ± 0.003 p		
Beam composition	0.169 ± 0.001 π^+ 0.025 ± 0.0007 K^+ 0.806 ± 0.002 p		

ELEVATION: FRONT PORTION OF MULTIPARTICLE SPECTROMETER
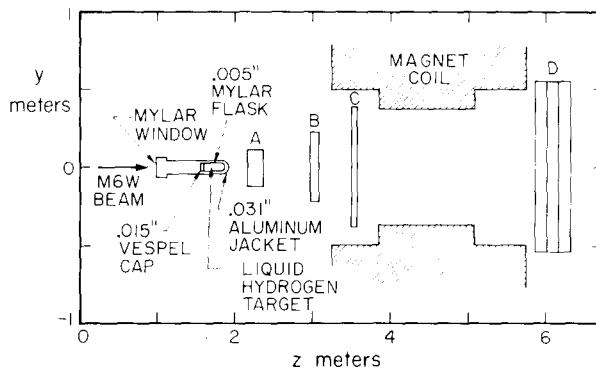
Fig. 2. Elevation view of front portion of E260 spectrometer.

The main E260 target was a cylinder of liquid hydrogen, 5.0 cm in diameter and 30 cm long. The downstream end of an aluminum vacuum jacket of thickness 0.08 cm, which was clearly separated from the hydrogen, served as an additional target for nuclear studies. The beam interaction probability (hydrogen and aluminum together) was about 5%. An elevation view of the target region is shown in fig. 2.

2.2. PROPORTIONAL CHAMBERS

Twenty-five proportional wire chamber planes, with a total of about 5000 wires, were used on this experiment. Three different constructions were employed, the characteristics of which are summarized in table 3. The proportional wire chambers had three functions in the event reconstruction. The chambers upstream of the target defined the position of incident beam particles. The one and two millimeter (wire spacing) chambers after the target were used to fit tracks before the magnet. The proportional wire chambers after the magnet sandwiched the higher resolution spark chambers, and were used to make roads (rough tracks) to speed up the

TABLE 3
Proportional chamber characteristics

	Type 1	Type 2	Type 3
Chambers	A	B, B', C	D, F', F''
Cathode wire spacing	$\simeq 1$ mm	$\simeq 2$ mm	$\simeq 5$ or 6 mm
Gas	Magic	Ar/CO_2	Ar/CO_2
Operating voltage	2700 V	4000 V	3500 V
Anode-cathode gap	$\simeq 3$ mm	$\simeq 7$ mm	$\simeq 10$ mm
Size	256 wires	56 or 320 or 512 wires	130 or 320 wires

track-finding algorithm after the magnet. They were also used to remove out-of-time tracks remembered by the spark chambers.

The beam position was determined with two groups of proportional wire chambers. Two x-planes (vertical wires) and two y-planes (horizontal wires) of type 2 were positioned thirty meters upstream of the hydrogen target. These chambers had 56 wires each. Five additional beam chambers were placed just upstream of the target. This group was comprised of two chambers of type 2 and three chambers of type 1. The type 2 chambers were 30° and 120° (with respect to the horizontal) skew planes of 56 wires each.

There were a total of eleven planes of wires between the target and the magnet (see fig. 1). Thirty centimeters downstream of the target were six planes of type 1. These chambers consisted of two x (AX, AXP), two y (AY, AYP), 45° and 135° skew (AU, AV) planes of 256 wires each. One meter downstream of the target were three planes of type 2. These chambers were made up of two x-planes of 512 wires each (BX, BXP), and one y-plane of 320 wires (BY). Two meters downstream of the target (just before the magnet) were two more planes of type 2, one x-plane of 512 wires (CX) and one y-plane of 320 wires (CY).

Directly after the magnet were two planes of type 3, an x-plane (DX) and a y-plane (DY) of 320 wires each. In front of each calorimeter were type 3 x-planes (FPR, FPL) of 130 wires each. Between the calorimeters was a type 3 x-plane of 320 wires (FPC).

2.3. SPARK CHAMBERS

Large magnetostrictive spark chambers were used for track finding after the magnet, and for the matching of x-tracks to y-tracks as discussed in sect. 4. Two sizes of chambers were used: E-chambers which were 2.5 by 1.5 m, and F-chambers which were 3.6 by 1.8 m. There were four E-modules and four F-modules, the locations of which are shown in fig. 1. Each module consisted of four planes of wires, a y-y spark gap and an x-u (or x-v) spark gap, the u (v) wires being at a stereo angle of 99.7 mrad (-99.7 mrad) with respect to the vertical. The wires were 0.005 inch diameter aluminum, spaced 32 to an inch. The gas mixture was 90% neon, 10% helium, and a trace of ethanol. For each module, x, y, and u (v) wands were read out from both ends; up to fifteen sparks were digitized from each end of each wand. The chambers had both d.c. and pulsed clearing fields. The spark chamber dead time was 50 ms for this experiment. This enabled us to record about twenty events per spill, with a dead time of about 50%.

2.4. MAGNET

The MPS has a large superconducting magnet, with an aperture of 122 cm by 61 cm and maximum $\int \boldsymbol{B} \cdot \mathrm{d}l = 25$ kGm. During E260, the magnet was set at a strength of $\int \boldsymbol{B} \cdot \mathrm{d}l = 12.6$ kGm in order to reduce the trigger bias due to the transverse momentum kick (in x-direction of fig. 1) imparted to charged particles. This field
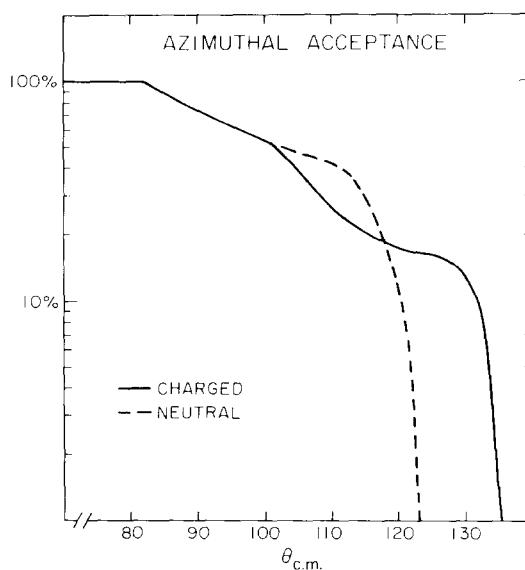
Fig. 3. The azimuthal (ϕ) acceptance as a function of c.m. polar angle (θ) for particles with 0.5 GeV c.m. energy.

strength corresponded to a transverse momentum kick of ± 379 MeV/c for charged particles. The resulting momentum resolution was $\Delta p/p = 0.0007p$ (GeV/c)$^{-1}$. The magnet aperture was the limiting factor in the azimuthal acceptance of the spectrometer. Fig. 3 shows this acceptance versus c.m. polar angle (not including calorimeter acceptance) for both neutral particles and charged particles of typical 0.5 GeV c.m. energy.

2.5. CALORIMETERS

The calorimeter design has been described in ref. [2]. Each calorimeter consisted of four modules of size 21 by 160 cm. Each module was divided into electromagnetic and hadronic sections. The electromagnetic section was made up of six strips of $\frac{1}{2}$ inch lead clad with $\frac{1}{16}$ inch steel alternating with $\frac{1}{4}$ inch scintillator (NE102), making a total of 14 radiation lengths and 0.4 absorption lengths. The six scintillators were viewed by one phototube at the top and another at the bottom. The hadronic section consisted of fifteen strips of two inch iron alternating with $\frac{1}{4}$ inch scintillator, for a total of 4.6 absorption lengths. The fifteen scintillators were viewed by top and bottom phototubes, as in the electromagnetic portion.

The calorimeters were centered at a laboratory angle of 100 mrad. This corresponded to approximately 90° in the c.m.s.*. The kinematic region covered by each of the calorimeters and the whole spectrometer is shown in fig. 4.

---

* For the 130 GeV/c running, the calorimeters were moved to a greater laboratory angle to correspond to 90° in the c.m.s.
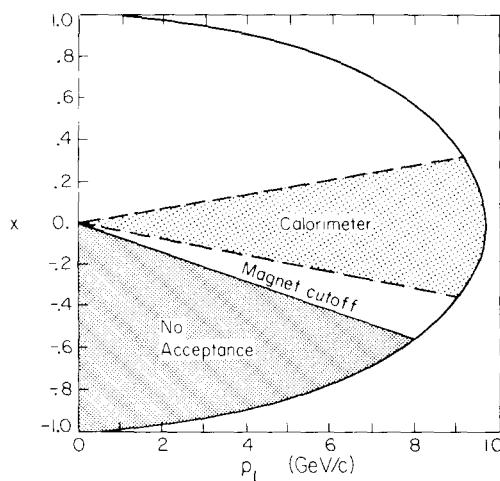
Fig. 4. The kinematic range in terms of Feynman x and $p_\perp$ covered by this experiment.

The calorimeters were calibrated by directing momentum analyzed beams of 10, 25, and 40 GeV/c charged particles into each module. As expected, the top (T) and bottom (B) pulse heights were found to be related to the energy (E) and vertical position (y) of the beam as measured from the center of the calorimeter by: $E \propto \sqrt{TB}$ and $y \propto \ln(T/B)$. This result is shown in fig. 5. The energy resolution (sigma) was determined to be: $\Delta E/E = 0.33/\sqrt{E}$ for electrons and $\Delta E/E = 1.03/\sqrt{E}$ for hadrons, where E is measured in GeV. The y coordinate resolution was determined to be: $\Delta y/y = 0.15/\sqrt{E}$ for electrons, and $\Delta y/y = 0.43/\sqrt{E}$ for hadrons. The calibration was checked offline on a run by run basis. To avoid

LINEARITY OF CALORIMETER RESPONSE
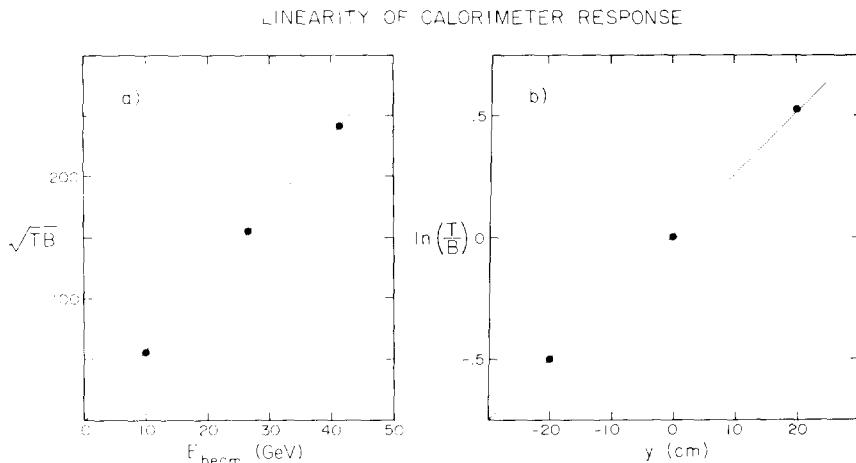
Fig. 5. Calorimeter calibration data; T and B represent top and bottom signals from a single calorimeter module.
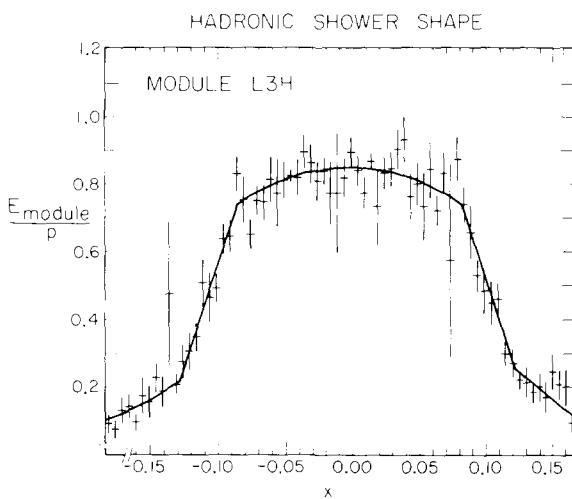
Fig. 6. The fraction of energy deposited in a single calorimeter module as a function of horizontal position measured with respect to the module center ($x = 0$.).

any trigger bias, events were selected which had a single charged hadron with momentum greater than 5 GeV/c entering the calorimeter opposite the trigger side. The ratio E/p was monitored, where p was the charged particle momentum and E was the energy deposited in the calorimeter. These events were also used to study hadronic shower size in our calorimeters. Fig. 6 shows the fraction of energy deposited in a single module as a function of horizontal distance from the center of the module. The peak value of 85% agrees with the calibration runs, where the beam was positioned at the module centers, and with previous measurements of hadronic shower sizes [9]. This shower information was not only extremely useful in the Monte Carlo simulation, and in the neutral particle determinations [10], but also served as an absolute calibration of calorimeter position.

3. Triggers

We recorded three different types of triggers, which we have labeled as interacting beam, single particle, and jet. The interacting beam trigger was defined to be: $A \cdot B \cdot \overline{C} \cdot \overline{D}$, where A and B were one inch square scintillation counters placed just before the target, C was a two inch square scintillation counter placed next to A and B with a $\frac{3}{4}$ inch hole cut in the center to veto beam halo, and D was a two inch square scintillation counter aligned with the beam and placed twelve meters downstream of the target. The interacting beam trigger also served as the pretrigger for the jet and single particle triggers. An alternate pretrigger (used in our earlier beryllium target runs, but not in these runs [2]) showed that the interacting beam trigger was 95% efficient when three or more charged particles were produced. The Monte Carlo jet events which are fully described in sect. 5 had a pretrigger

efficiency of 98%. An interacting beam event was written to tape after every nine jet or single particle triggers, throughout the data taking. A total of 50 000 of these interacting beam events were recorded. Jets with $p_\perp$'s of up to 3 GeV/c were obtained from this data sample which had no high $p_\perp$ trigger requirements. This was useful in checking the acceptance of the calorimeter triggered jets.

The single particle trigger was characterized by a large signal in one or more calorimeter modules. For each calorimeter module, we summed up the top and bottom electromagnetic and hadronic signals (four total). This sum was then attenuated by an amount proportional to the mean horizontal laboratory angle of the module, to give a signal approximately proportional to transverse momentum. If a particle hit the calorimeter at a vertical distance y from the module center, the trigger $p_\perp$ estimate was low because we had underestimated the angle. This was partially compensated by an overestimate in the energy. The true energy was proportional to the geometric mean of top and bottom pulse heights, but the trigger electronics calculated the arithmetic mean, which is always greater than the geometric mean. The net result of this was that for particles displaced 40 centimeters vertically, the average $p_\perp$ response of the electronics was 6% low (below true $p_\perp$) for module one, 3% low for module two, 1.5% low for module three, and 0.5% low for module four. The single particle trigger required a minimum signal in one of eight possible calorimeter modules. Data at two different biases were taken together. Only a small fraction (2–4%) of the lower bias triggers were recorded, so that the two triggers were live about the same amount of time.


RAW $p_\perp$ DISTRIBUTIONS
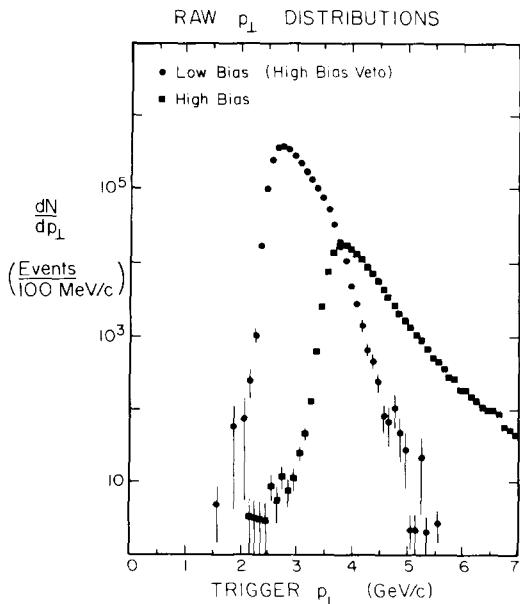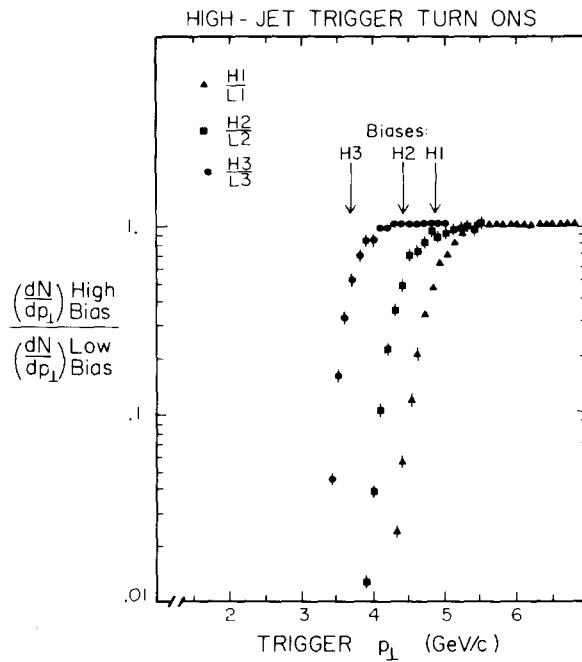
Fig. 8. The ratio of high bias to low bias (reconstructed calorimeter trigger $p_\perp$) which shows the sharpness of the trigger.

For the jet trigger, the electronics summed up the four single module $p_\perp$'s on each side. The total $p_\perp$ in a single calorimeter (left or right side) was required to be above the preset trigger bias. As with the single particle triggers, data at two different biases were recorded together. Three different pairs of biases were selected. We have recalculated the hardware jet $p_\perp$ with the sixteen recorded calorimeter signals. Fig. 7 shows calorimeter raw $p_\perp$ distribution for high and low jet samples with a typical bias. It should be noted that each calorimeter signal was digitized in proportion to the integral of the pulse, whereas the trigger hardware discriminated on one net pulse height. Hence, the triggers do not have a perfectly sharp onset. For each pair of triggers recorded together, one bias was much lower than the other. This means that in the $p_\perp$ region of the higher bias, data from the lower bias trigger were essentially unbiased. Fig. 8 shows a plot of high bias divided by low bias (recalculated hardware $p_\perp$). These curves show the sharpness of the trigger, and were used in calculating the trigger acceptance described in sect. 5.

4. Event reconstruction

4.1. CHARGED PARTICLES

Due to the high multiplicity of charged particles in the events which trigger the apparatus, the pattern recognition was difficult in this experiment. The track-finding

described below took the bulk of the computer time needed for event analysis. Tracks were found independently in the x and y views before being matched to each other using the skew chambers. Software was developed in order to optimize the track-finding algorithm [11]. Chambers were divided into groups, and a minimum number of hits were required in each group. The program took pairs of hits in different groups to define a one centimeter wide road. If the total number of chamber hits in the road satisfied group hit requirements, a least-squares fit was done using all hits in the road. The program then deleted the hit with the largest residual, while still satisfying group hit requirements, and then refit the track. A track was accepted as being genuine if at any stage the chi-squared per degree of freedom (χ^2) was less than 2.5. Tracks were also accepted if the χ^2 was less than 5.0 with the minimum chamber requirements (no possibility of deleting any hits). If two accepted tracks were within five mrad of each other, only the track with the best fit was kept.

Table 4 defines the grouping of chambers (see fig. 1). The first step was to find the vertex. Tracks were fit in the non-bending y-z view (y-tracks) demanding $\geqslant 1$ hit in group Y1, $\geqslant 1$ hit in group Y2, $\geqslant 2$ hits in group Y3, and a total of $\geqslant 5$ hits in groups Y1, Y2, and Y3 together. Tracks were fit in the x-z view (x-tracks) before the magnet demanding $\geqslant 1$ hit in group X1, and $\geqslant 2$ hits in group X2. The best of these x and y tracks were selected on the basis of being at wide-angle (for good vertex z resolution), having low χ^2, and having a high number of chambers hit. These selected tracks were used to fit the vertex position in three dimensions. In the case that the above algorithm failed, a second iteration was made, forcing the selected tracks to agree with beam chamber information (two dimensional). Clean vertices were reconstructed in the target region on 77% of the jet triggers. A vertex distribution is shown in fig. 9. The peak at $z = 1.58$ m is due to the mylar entrance

TABLE 4

Chamber group definitions

| Group name	Chambers in group
Y1	AY, AYP
Y2	BY, CY
Y3	DY, EY1, EY2, EY3, EY4
Y4	FY1, FY2, FY3, FY4
X0	AU, AV
X1	AX, AXP
X2	BX, BXP, CX
X3	DX, EX1, EX2, EX3, EX4
X4	FX1, FX2, FX3, FX4, FPR, FPL
X5	FPC
S1	EU2, EU4, FU1, FU2
S2	EU1, EU3, FU3, FU4
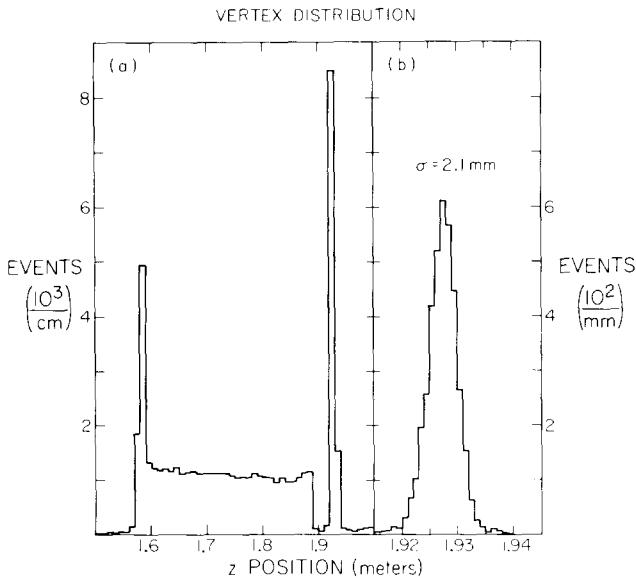
Fig. 9. Reconstructed vertex position; only the region $1.6 < z < 1.88$ m was used to select a clean target proton.

window. The liquid hydrogen extends from $z = 1.59$ m to $z = 1.89$ m. The peak at $z = 1.93$ m is due to the thin aluminum vacuum jacket. This determines the z resolution of the vertex to be 2.1 mm.

At this stage, good knowledge of the vertex allowed track finding to be done with less stringent chamber requirements than would otherwise be necessary. y-tracks were then fit demanding agreement with the vertex, $\geqslant 1$ hit in group Y1, $\geqslant 1$ hit in group Y2, and $\geqslant 3$ hits in group Y3. "Super" x-tracks after the magnet were fit demanding $\geqslant 3$ hits in group X4, and $\geqslant 8$ hits total. The hits used by the super tracks were then deleted, except those in the DX, FPR, and FPL chambers which have coarse wire spacing. Additional x-tracks after the magnet were then fit demanding $\geqslant 3$ hits in group X3, $\geqslant 2$ hits in group X4, and $\geqslant 6$ hits total. Track-finding after the magnet was completed by making a third pass for wide-angle x-tracks by requiring $\geqslant 4$ hits in groups X3 and X5 combined.

The x-tracks after the magnet were then matched to the y-tracks using the stereo-angle spark chambers. Matching requirements were: $\geqslant 1$ match in group S1, $\geqslant 1$ match in group S2, and $\geqslant 4$ matches total. x-tracks were then found before the magnet. These tracks were required to pass through the vertex, link up to a track downstream of the magnet, and have a total of $\geqslant 3$ hits in groups X0, X1, and X2 together. At this point we had a set of matched tracks (particles) which was complete, but was loose in the sense that two particles could share one view (e.g., two x-tracks may have been matched to the same y-track). We looked at all such combinations of view-sharing, and deleted the worst particle on the basis of chi-squared of match and number of matches [12].

Each of the calorimeters subtended a solid angle of 0.9 sr in the c.m., and detected both hadronic and electromagnetic (i.e., π^0's) neutrals which entered them. The major problem was to separate upward fluctuations in energy deposited in the calorimeters by charged particles from actual neutrals. This is especially serious on the trigger side, as we have pointed out previously [2]. For each charged particle entering a calorimeter, we predicted how much energy (from fig. 6) would be detected in each of the four modules. We summed over all charged particles in the event to get the net predictions for each module. If the observed calorimeter energy exceeded the charged particle predictions, we had a neutral particle candidate. We then tried to fit for f_h, the fraction of energy deposited in the hadronic section, with the assumption that there were no neutrals present. This fit had three degrees of freedom because there were four pieces of data, top and bottom electromagnetic and hadronic pulse heights, and one unknown, f_h. For the cases where this fit was successful (no neutral present), we found the mean value of excess calorimeter energy ($\bar{E}$) to be zero on the away side. This was expected because there was no trigger bias on the away side and charged particles fluctuate high or low in their energy response with equal probability. We found $\bar{E}$ greater than zero for these same events on the trigger side, which arises from the high-$p_\perp$ trigger favoring upward fluctuations in calorimeter response. The f_h determined in this fit agreed with measured f_h from beam calibration runs. If the all charged particles fit failed, we tried to fit the module with the addition of a pure hadronic neutral or a pure electromagnetic neutral. This fit had one degree of freedom because there were three unknowns: the neutral particle energy, the neutral particle vertical position, and f_h for charged particles. If both of these fits failed, we then assumed that both hadronic and electromagnetic neutrals were present, and their energies were calculated by simple subtraction.

4.3. EVENT CLEANUP

We have made a detailed study of the reliability of our events [10]. This study was broken into two parts: individual particle quality and overall event quality. The particle quality study was aimed at getting rid of particles which may have been created by the software in complicated high-multiplicity events. The purpose of the event quality study was to eliminate entire events which were likely not to have been high-$p_\perp$ events at all. To investigate particle reliability we calculated a set of twelve quality variables, p_i ($i = 1, 12$). These variables were functions of the number of chambers registering hits along particle tracks, and the track chi-squares. The p_i were constructed such that low p_i corresponded to less-certain particles (e.g., small number of chamber hits and high chi-square in track fitting) and high p_i corresponded to particles which were more likely to be real. In a similar fashion, we defined eight variables, e_i ($i = 1, 8$), to represent the overall quality of the event.

The procedure was to compare the quality number distributions (dN/dp_i and dN/de_i) from the total data sample to the distributions expected for real particles and events. To do this we needed a set of particles and events which had a very high probability of being real. We defined our special sample of real events as those events in which: (i) the total visible energy in the spectrometer was less than the beam energy, (ii) all charged particles which entered the calorimeters had momenta which agreed with the calorimeter energy measurement, and (iii) the vertex was successfully fitted on the first pass (see subsect. 4.1) with coordinates which agreed very well with the beam chamber hits. This sample of select events was about 36% of the total data sample. Our special sample of good particles were defined to be those particles which: (i) belonged to a good event as defined above, and (ii) hit a calorimeter so that its energy was well verified.

We then constructed the functions:

$$F(p_i) = C \frac{(dN/dp_i)_{\text{good sample}}}{(dN/dp_i)_{\text{total sample}}},$$

where C is a normalization constant. One grand measure of particle quality, Q_p, was then defined to be:

$$Q_p = \prod_i \frac{F(p_i)}{1 - F(p_i)}.$$

A minimum value of Q_p was imposed for allowing a particle to be accepted in the final analysis. We removed 6% of our particles with this cut. Applying the same cut to our special sample of good particles removed only 1% of these. Similarly, one net measure of event quality, Q_e, was constructed. We removed 6% of our hydrogen target events with a cut on Q_e, and note that about one-half of the events removed by this cut had vertices in the target vacuum region ($z = 1.9$ m of fig. 9).

5. Monte Carlo and jet definition

The quantum chromodynamic approach of Feynman, Field, and Fox [7] was used as the starting point for modeling high-$p_\perp$ jet events. In this theory hadron jets arise from the following two-body processes: $qq \rightarrow qq$, $q\bar{q} \rightarrow q\bar{q}$, $\bar{q}\bar{q} \rightarrow \bar{q}\bar{q}$, $qg \rightarrow qg$, $\bar{q}g \rightarrow \bar{q}g$, $gg \rightarrow q\bar{q}$, $q\bar{q} \rightarrow gg$, and $gg \rightarrow gg$. We summarize here the ingredients of this QCD approach. The unknown scale factor Λ, which is related to the strong interaction coupling constant by

$$\alpha_s \simeq \frac{12\pi}{25 \ln(Q^2/\Lambda^2)},$$

was fixed at 0.4 GeV/c. This is consistent with the analysis of scale breaking in ep and μp interactions [13–16]. The distributions of quarks and gluons in the proton, $G(x, Q^2)$, were determined from fits to ep and μp data. The gluon distribution was relatively unconstrained by these fits; gluons take up about 50% of the proton momentum. The transverse momentum distribution ($k_\perp$) of quarks and gluons in the proton was taken to be gaussian, with $\langle k_\perp \rangle$ (mean absolute deviation from zero) equal to 0.85 GeV/c. This agrees with the data on muon pair production in pp collisions [17]. The relative cross sections of the quark and gluon two-body processes were put in as calculated from QCD first-order perturbation theory by Cutler and Sivers [18], and by Combridge, Kripfganz, and Ranft [19].

Four jets appear in the final state. The scattered constituents define the axis of the trigger and away side jets, and the beam and target remnants define the axis of two additional jets. Mean jet momentum vectors are shown in fig. 10 for the proton-proton case. The dashed boxes, which give a rough idea of the variation of these vectors from event to event, contain roughly two-thirds of the events. The rather large momentum difference between the trigger jet and the away jet is due entirely to the primordial transverse momentum of partons inside the proton. The trigger tends to select those events in which one of the proton constituents is already headed in the trigger direction. The transverse momentum is balanced (in the proton-proton c.m.s.) by the tilting of the beam and target jets. This is shown
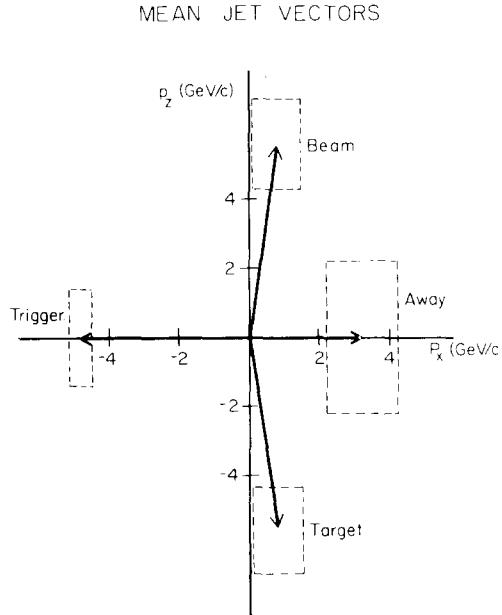
MEAN JET VECTORS

Fig. 10. Mean jet momentum vectors defined by two-body QCD scatters of ref. [7]. The boxes indicate where roughly two-thirds of the events are.
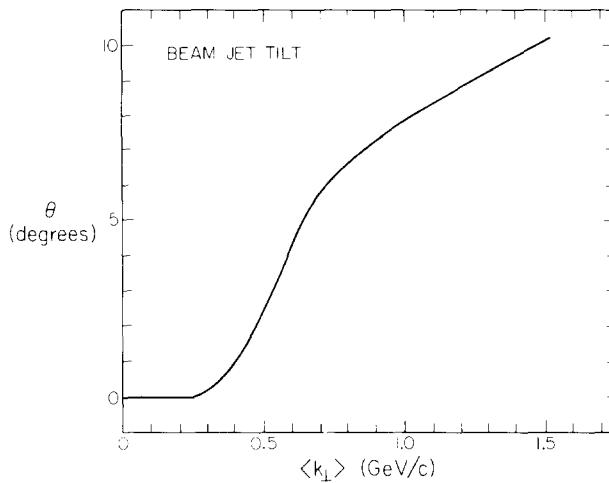
Fig. 11. Amount of beam jet tilt as a function of parton transverse momentum.

quantitatively in fig. 11, where we plot the amount of beam jet tilt as a function of the amount of primordial transverse momentum of partons inside the proton. The invariant cross section for producing a typical 5 GeV quark at 90° in the c.m. is also sensitive to this choice of parton $\langle k_\perp \rangle$. This is shown in fig. 12.

The two scattered partons, the beam remnants, and the target remnants were then each fragmented into a jet of hadrons using a jet generator developed by Field and Feynman [20–22]. Their jet maker fragments a parton of specified flavor and momentum into a jet of hadrons. Even in this simple picture there may be more
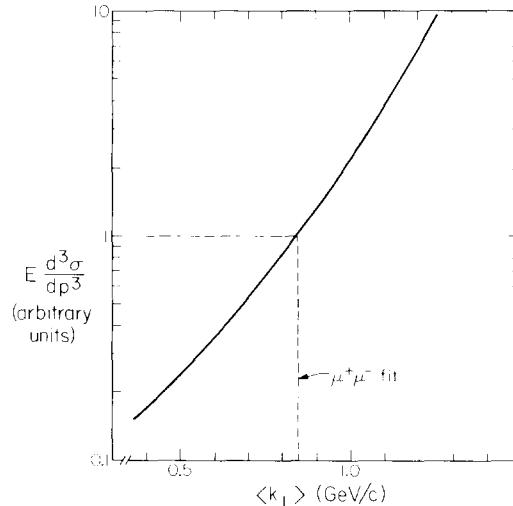
Fig. 12. Dependence of invariant jet cross section on parton transverse momentum.
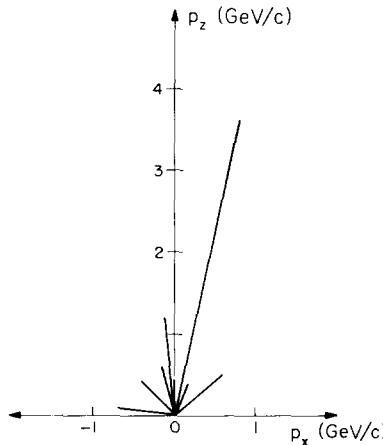
Fig. 13. Typical parton fragmentation for a 5 GeV quark.

than one quark left in the beam or target after the scatter. In these cases, we randomly chose one of the remaining quarks to be fragmented*. In any case, the parton being fragmented carries the total momentum of the beam or target remnant. The quark fragmentation functions, $D(z, Q^2)$, were fixed such that the final distribution of hadrons agreed with lepton experiments [23–24]. Pseudoscalar and vector mesons were produced with equal probability; no baryons were produced. The gluon fragmentation functions were chosen to be arbitrarily softer than the quark fragmentation functions. This is needed to fit the high-$p_\perp$ ISR data on the away side [25]. Scale breaking (Q^2 dependence) in the fragmentation was not included; we have more to say about this in sect. 7.

A typical 5 GeV quark fragmentation is shown in fig. 13. For a 5 GeV jet, a significant amount of energy appears in masses of the jet fragments (hadrons) and the transverse momenta of these fragments about the jet (parton) direction. This means there is a rather large difference between jet $p_\perp$ and jet energy**. This is shown quantitatively in fig. 14. Here we plot the cross section for producing a quark or gluon of given energy (solid line) along with the resulting cross sections versus $p_\perp$ after fragmentation (broken lines). The energy cross section comes from QCD [7]; the $p_\perp$ cross sections depend, in addition, on the choice of fragmentation functions.

The Monte Carlo events were tracked through the spectrometer apertures and the calorimeter response was simulated. For each hadron and photon of energy, E,

---

* The exception is that if a gluon scatters, we fragment the remnants as a gluon.
** Jet energy is not a meaningful concept experimentally (at least at present energies) because missing a single soft particle can significantly alter the energy, while it would not greatly affect the $p_\perp$.
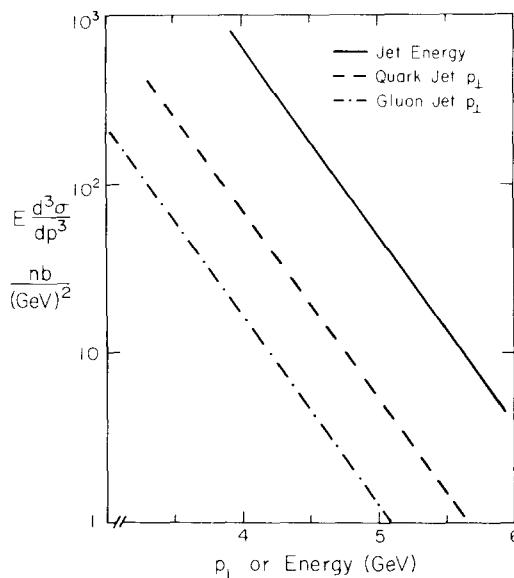
Fig. 14. The effect of parton fragmentation on the invariant cross section when jet $p_\perp$ (as opposed to jet energy) is measured.

striking the calorimeter face at position, (x, y), we needed to predict the distribution of light seen by the sixteen phototubes. Photons usually generated signals in only two phototubes (top and bottom), because the shower width is much smaller than the width of a calorimeter module, and the probability of significant penetration of the fourteen radiation lengths of lead was small. However, a single hadron often generated signals in eight or more phototubes, because the shower width is about the same size as the width of a calorimeter cell, and the non-elastic hadronic interaction probability in the lead section was $\frac{1}{3}$.

The first step in the simulation of the calorimeter response was to generate an energy response, E', according to measured gaussian distributions. E' is not the final energy that appears in the calorimeter, for the entire shower may not be contained due to transverse or longitudinal leakage. Next a vertical calorimeter position response, y', was generated according to the measured gaussian distributions. The energy, E', was divided into a lead portion (E_e) and an iron portion (E_h) with: $E' = E_e + E_h$. For hadrons, the distribution of E/E' (E is the true particle energy) was taken as measured in the beam calibration runs. For photons, E_h was taken to be zero. The partitioning of energy from hadronic showers into the four modules was accomplished by using the measured shower information shown in fig. 6. The jet trigger $p_\perp$ was then calculated with the sixteen calorimeter signals according to the prescription given in sect. 3. Events were then selected according to the trigger probability curves of fig. 8, and written to magnetic tape in the same format as the real data.

We have used the Monte Carlo events to help determine a reasonable jet definition. Fig. 15 shows a plot of the angular distribution of all spectrometer accepted charged particles with c.m. energy greater than 0.5 GeV. The contributions of the trigger, beam, away, and target jets are plotted individually. There is a clear separation between the clusters of particles near 90° (along the trigger jet axis) and near 0° (along the beam jet axis). This clear separation is also seen in the data [26]. We defined a preliminary jet vector as the vector sum of all particle momenta entering a 45° cone centered at 90° in the c.m. The trigger forced this vector to be near 90°. We then defined the trigger jet to be the collection of all particles which were contained in a 40° cone whose axis coincided with the preliminary jet vector. This is the cone size which, on the average, balances the loss of trigger parton associated particles with the gain of non-trigger parton associated particles. The exact size of this cone does not affect the cross-section measurements reported in sect. 7 because the acceptance correction accounts for missing trigger jet particles and gaining background particles. If we had a calorimeter which was twice as large (2 sr), we would lower our apparent cross section by a factor of 7 with an analogous acceptance correction. For these cross-section measurements, the trigger jet vector (vector sum of the momenta of all trigger jet particles) was required to be in the fiducial region $|y| < 0.2$ and $|\phi| < 20°$, where y is the c.m. rapidity and ϕ is the azimuthal angle of the jet. These cuts help insure containment of the jet in the calorimeter. Fig. 16 shows a c.m. view of the 40° cone, the calorimeter, and the (y, ϕ) fiducial region. The cone is larger than the calorimeter, which means that we have neutral particle detection only in the important central region. Enlarging the jet definition region from the true calorimeter size to a 40° cone only increases the jet $p_\perp$ by an average of 100 MeV/c.
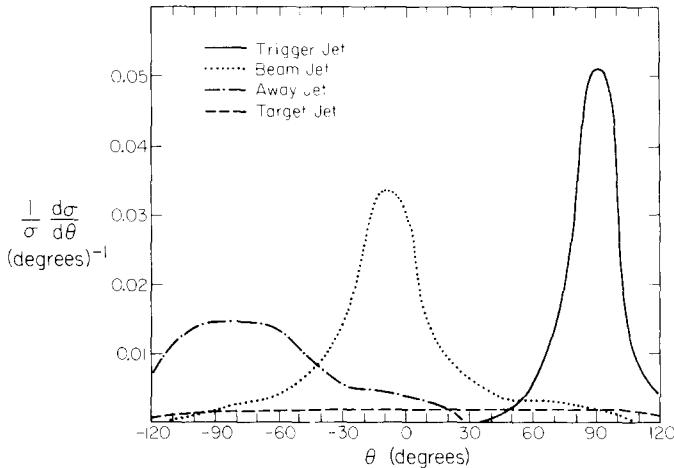

Fig. 15. Angular distribution of charged particles which are accepted by the spectrometer and have energy greater than 0.5 GeV in the c.m.; the four jets are plotted separately.

----- 40° Cone
——— Calorimeter
·········· Fiducial Region
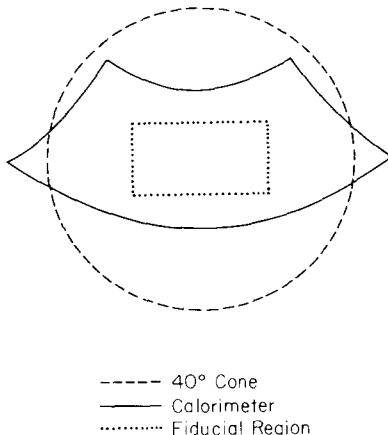
Fig. 16. Center of mass view of trigger calorimeter.

6. Event structure

6.1. DATA AND QCD MODEL COMPARISON

We have made a detailed comparison of these Monte Carlo events with our data. We define $z \equiv \boldsymbol{p} \cdot \boldsymbol{p}_j / |\boldsymbol{p}_j|^2$, where $\boldsymbol{p}$ is an individual charged particle momentum, and $\boldsymbol{p}_j$ is the trigger jet momentum (as defined in the sect. 5). Fig. 17 shows the z distributions of all charged particles passing spectrometer cuts for the Monte Carlo and the data. The plots are divided into trigger side ($z > 0$) and away side ($z < 0$). The trigger jet $p_\perp$ was required to be in the range $4 < p_\perp < 5$ GeV/c for these
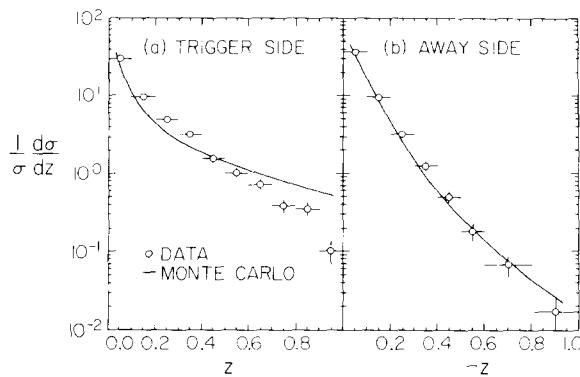

Fig. 17. Comparison of z distributions of charged particles between data and QCD Monte Carlo. The trigger jet $p_\perp$ is between 4.0 and 5.0 GeV/c.

plots. Fig. 18 shows the c.m rapidity distributions for the same events, data and Monte Carlo. Fig. 19 shows the distributions of transverse momentum (with respect to the beam axis) for the same events again. We stress that the Monte Carlo curves were not arbitrarily normalized to the data; the event multiplicities came out correctly (to 5%) from the model. The away side agreement is remarkable. The agreement between the model and the data is qualitatively good on the trigger side.
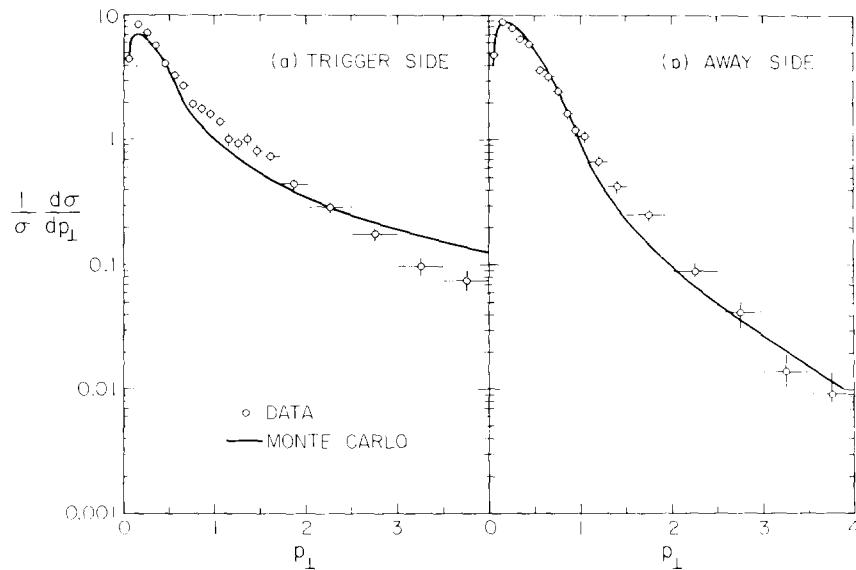
Fig. 18. Comparison of c.m. rapidity distributions of charged particles between data and QCD Monte Carlo. The trigger jet $p_\perp$ is between 4.0 and 5.0 GeV/c.
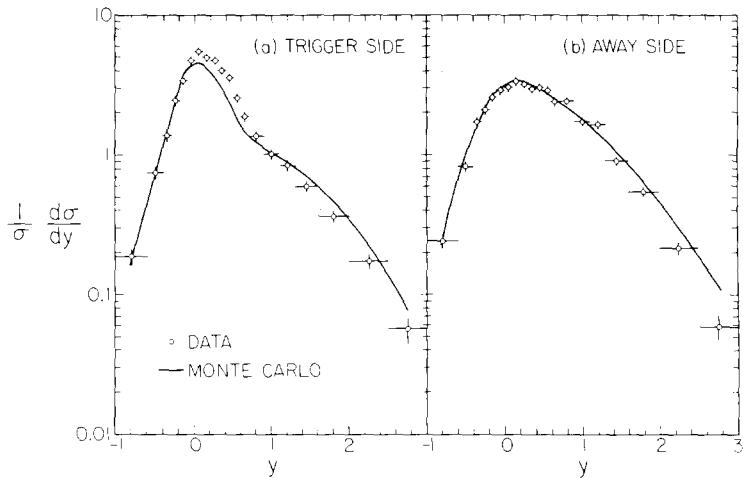
Fig. 19. Comparison of $p_\perp$ distributions for charged particles between data and QCD Monte Carlo. The trigger jet $p_\perp$ is between 4.0 and 5.0 GeV/c.
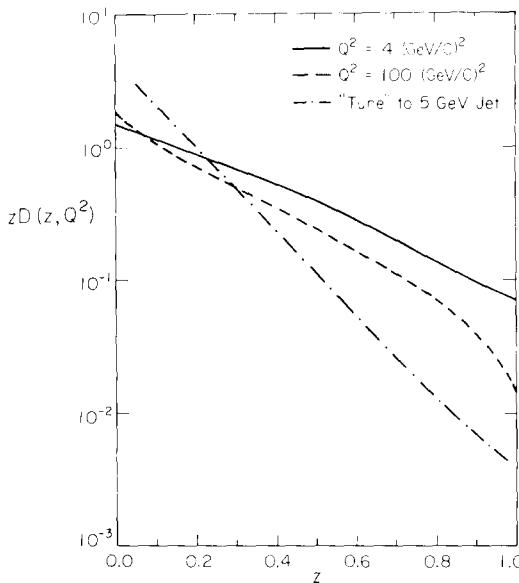
Fig. 20. Fragmentation function for up quark→charged hadron from ref. [7] for $Q^2 = 4$ (GeV/c)^2 (solid curve) and $Q^2 = 100$ (GeV/c)^2 (dashed curve). Also shown (dot-dash curve) is a fragmentation which would fit a 5.0 GeV/c jet measured in this experiment.

However, the data show a softer (fewer high $p_\perp$ particles) distribution of charged hadrons than the Monte Carlo. In earlier work [4], we suggested that this was not a problem for QCD because the fragmentation functions used in the Monte Carlo were determined at $Q^2 = 4$ (GeV/c)^2 and the jet data correspond to much larger Q^{2*}. To investigate this in detail, we arbitrarily adjusted the input parton fragmentation such that the final-state distribution of charged hadrons agreed with the E260 jet data. The fragmentation function for parton→(charged hadron) which produces agreement with our jet data at $p_\perp = 5$ GeV/c is shown in fig. 20 (dash-dot curve). Also shown are the $Q^2 = 4$ (GeV/c)^2 "standard" for (up quark) →(charged hadron) from ref. [7] (solid curve). Scale breaking in QCD softens this fragmentation at higher values of Q^2. The QCD leading log prediction of ref. [7] for $Q^2 = 100$ (GeV/c)^2 is shown (dashed curve). The proper Q^2 corresponding to our jet events is not known. It is certainly much larger than 4 (GeV/c)^2 and we may only guess that $Q^2 \sim 4p_\perp^2 \sim 80$ (GeV/c)^{2*}. In spite of this uncertainty, it is clear that our higher $p_\perp$ jets are described by a softer fragmentation function than the $Q^2 = 100$ (GeV/c)^2 up quark fragmentation function of fig. 20. If our trigger jets are from gluons as well as quarks, and if the gluon fragmentation at high z is much softer than the quark fragmentation, then this could account for the data. However, the problem with this is that softening the gluon fragmentation would also lower the cross section for producing a jet of specified $p_\perp$, as explained in sect.

---

* For instance, lower $p_\perp$ jets measured on this experiment have a fragmentation (z distribution) which agrees fairly well with the $Q^2 = 4$ (GeV/c)^2 fragmentation.
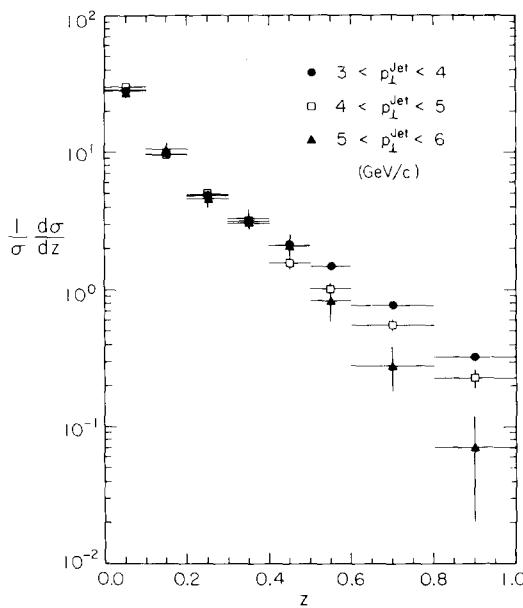
Fig. 21. Trigger side z distributions for charged particles as a function of trigger jet $p_\perp$.

5. Thus, it seems that a large percentage of gluons ($\approx 80\%$) would be needed to get agreement with the data. We conclude the discrepancy shown in fig. 20 is a significant disagreement with the theory.

We have direct evidence for scale breaking (Q^2 dependence) in hadronic interactions. Fig. 21 shows the z distributions for three different jet $p_\perp$ bins: 3–4, 4–5, and 5–6 GeV/c. The Q^2 of these events are roughly 50, 80, and 120 (GeV/c)^2, respectively*. The higher $p_\perp$ jets are less likely to have a single charged particle taking up 50% or more of the total jet momentum. This effect is predicted by QCD; the harder struck quarks are more likely to radiate gluons. Considerable effort has gone into making sure that the Q^2 dependence seen in fig. 21 is not due to an acceptance effect. Monte Carlo events with a constant fragmentation (independent of quark energy) were run through the analysis software. The events were plotted in the same jet $p_\perp$ bins as the data. The result was that the curve of fig. 17a was always produced, independent of jet $p_\perp$, so that selecting a high analyzed jet $p_\perp$ did not distort the output z distribution. Random soft particles were added to the Monte Carlo events to see if changing the background contribution of non-trigger jet particles could produce such an effect. The inclusion of several extra particles did not significantly alter the Monte Carlo prediction of fig. 17a. Another reassuring check of the data was the fact that the total fraction of the jet $p_\perp$ in charged particles was constant, independent of jet $p_\perp$. Further evidence for scale breaking in the form of jet broadening is also seen clearly in fig. 22. Here we plot

---

* This assumes that $Q^2 \sim s$. If $Q^2 \sim t$, then the Q^2 are a factor of two lower. Q^2 is uncertain to at least this level.

MEAN $k_\perp$ OF JET FRAGMENTS
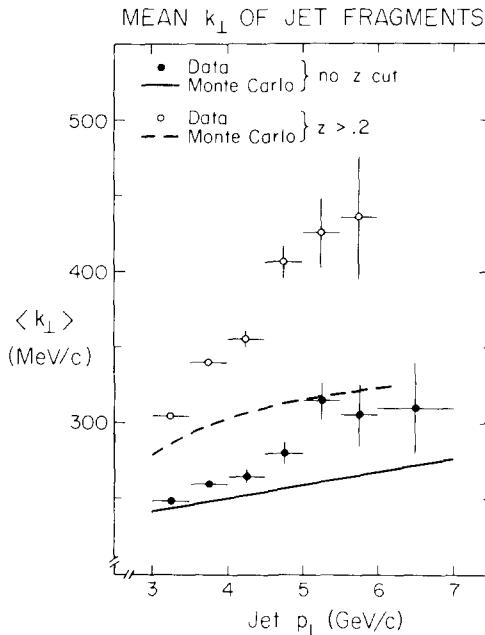
Fig. 22. Mean charged particle momentum transverse to the jet ($\langle k_\perp \rangle$) as a function of trigger jet $p_\perp$ compared to the Monte Carlo which had constant $\langle k_\perp \rangle$ versus jet $p_\perp$.

the mean transverse momentum of charged particles with respect to the jet axis as a function of jet $p_\perp$, and note an increase in this mean transverse momentum with increasing jet $p_\perp$. Making a cut of $z > 0.2$ to suppress background (soft particles) enhances the effect. The Monte Carlo curves are the predictions for no scale breaking; the gentle rise is due to acceptance.

6.2. CHARGED PARTICLE CORRELATIONS

Fig. 23 shows the ratio of inclusive charged particle distributions as a function of z (trigger jet momentum fraction) for pp, $\pi^+ p$, and $\pi^- p$ jet events. The data are divided into three trigger jet $p_\perp$ bins and separated into trigger and away sides. The pp and $\pi^+ p$ data on both the trigger and away sides show a clear decrease in the negative to positive ratio with increasing $|z|$. The ratio is about 0.9 at low $|z|$ and decreases to about 0.3 at high $|z|$. The high $|z|$ particles presumably come predominantly from quark fragmentation. The quark jets in pp and $\pi^+ p$ events are dominated by the up (and $\bar{d}$) quarks which fragment preferentially into positively charged leading (high z) particles. No significant dependence on trigger jet $p_\perp$ is seen. The ratio of number of negatives to positives in $\pi^- p$ jet events is observed to be roughly 1, independent of z, on both the trigger and away sides. Also no dependence on trigger jet $p_\perp$ is seen for the $\pi^- p$ events.

The theoretical curves in fig. 23 are from ref. [7]. For comparison with the data on the trigger side, the theoretical curve (solid line) is the contribution from the
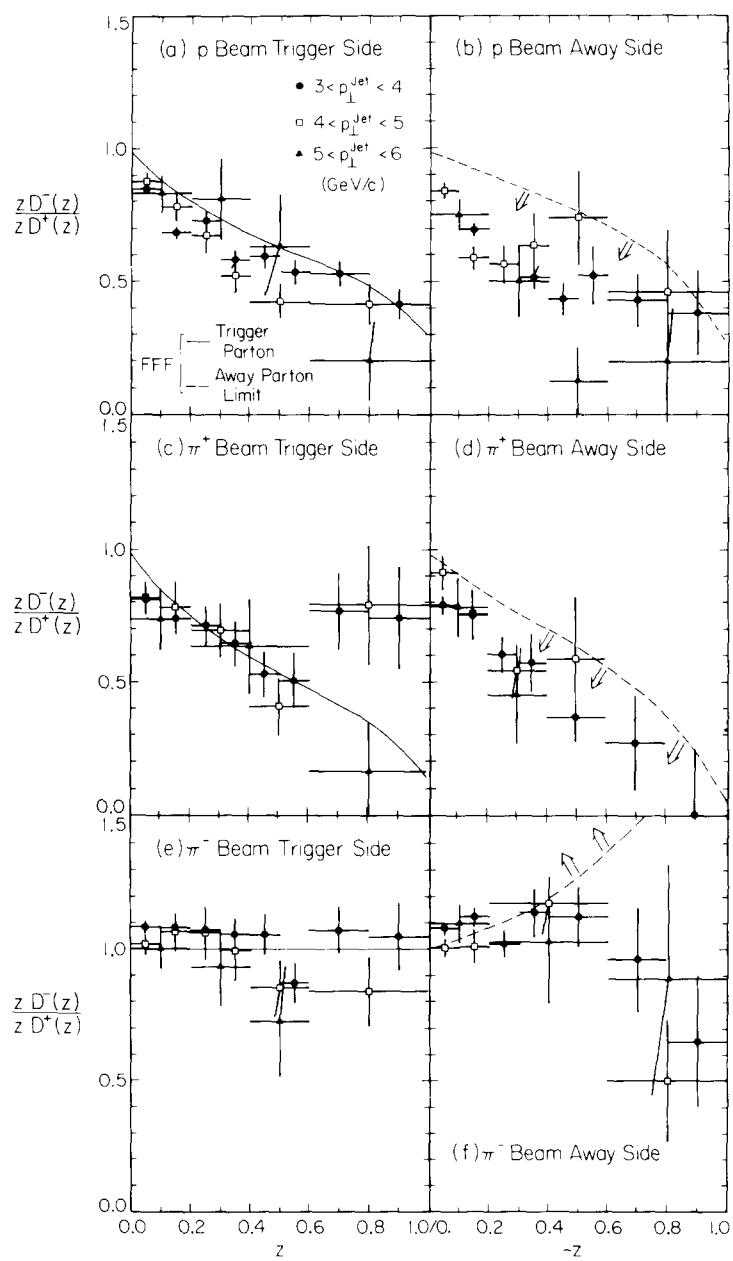
Fig. 23. The negative to positive charge ratio as a function of z (jet momentum fraction) for p beam (a, b), π^+ beam (c, d), and π^- beam (e, f).
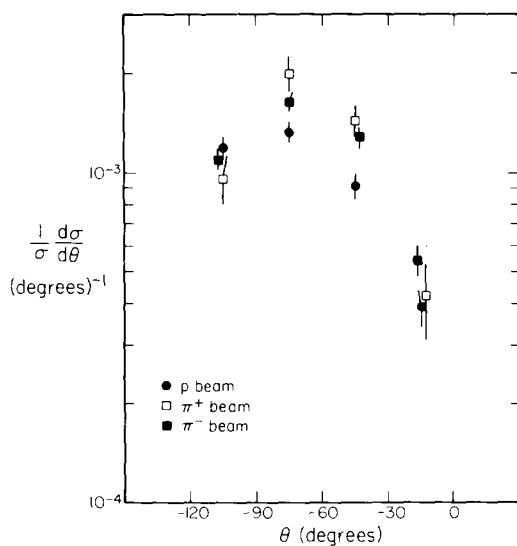
Fig. 24. Away side angular distribution of charged particles with $p_\perp$ greater than 1.6 GeV/c when the trigger jet $p_\perp$ is greater than 3.0 GeV/c.

trigger parton only. The beam jet would introduce a background at low z. The theory accounts reasonably well for all three beam types on the trigger side. For comparison with the away side data, the theoretical curve (dashed line) is the contribution from the away parton only. However, the theoretical z is calculated with respect to the away parton momentum, whereas the data uses the trigger jet momentum. Since the trigger parton momentum is on the average substantially larger than the away parton momentum due to the parton transverse momentum (see fig. 11), we plot the theory as a limit on the away side[*]. The pp and π^+ p away side data are in agreement with this theoretical bound. However, the π^- p data show a rather large disagreement with theory. The theory predicts an excess of high $|z|$ negative particles on the away side which is not observed in the data. This theoretical prediction seems natural because the pion quark is believed to have a greater momentum, on the average, than the proton quark. Therefore, the pion quark is likely to be directed forward in the pion-proton c.m.s. after the scatter. An event with a 90° trigger would then have an excess of pion quarks on the away side in this simple picture[**].

Fig. 24 shows the away side angular distribution[***] of all charged particles with $p_\perp$ greater than 1.6 GeV/c. The trigger jet $p_\perp$ was required to be above 3 GeV/c.

[*] To do a detailed Monte Carlo (as was done in the pp case) for all the beams would require too much computer time. We felt this was not profitable in as much as relatively little is known about the structure of the pion.

[**] Remember that our acceptance is larger in the forward hemisphere.

[***] θ is the "projected" polar angle (in the plane defined by the beam axis and the trigger jet axis). See ref. [26].
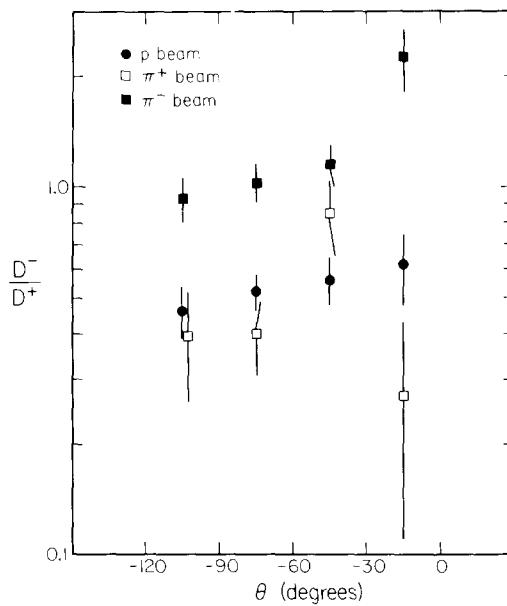
Fig. 25. Away side negative to positive charge ratio as a function of c.m. angle for particles with $p_\perp$ greater than 1.6 GeV/c. The trigger jet $p_\perp$ is greater than 3.0 GeV/c.

Thus, an away side particle with $p_\perp$ greater than 1.6 GeV/c has a large probability of having arisen from the away parton. Data are shown for p, π^+, and π^- beams. At $-75°$ and $-45°$ (forward angles) the π^+ and π^- beams are seen to produce more high $p_\perp$ particles than the proton beam. This is most likely a consequence of the fact that for the pion beams, the parton-parton c.m.s is moving forward relative to the pion-proton c.m.s. For these same events with high-$p_\perp$ away side particles, fig. 25 shows the ratio of the number of negative charges to positive charges ($p_\perp > 1.6$ GeV/c) as a function of away side angle. The data from p, π^+, and π^- beams are all consistent with no change in this ratio from $-120°$ to $-30°$. The rise at $-15°$ for the π^- beam data is attributed to contributions from the beam jet.

7. Acceptance and cross sections

Having succeeded in modeling the event structure, the Monte Carlo events were used to study the jet acceptance of our apparatus. It was not just as simple as individual events being accepted or not accepted. Jet $p_\perp$'s were not measured with perfect resolution. There was also the problem of wide angle soft fragments from the trigger parton missing the 40° trigger jet cone, and soft fragments from the beam entering the trigger jet cone. The result is that a trigger which arises from a parton of transverse momentum $p_\perp$ appears in our data as a jet with transverse momentum close to $p_\perp$, but not exactly equal to $p_\perp$. To calculate the jet acceptance (as a function of $p_\perp$), one needs to generate events over the entire $p_\perp$ range

of interest. Events were generated in the $p_\perp$ range 2.0 to 7.0 GeV/c with a $p_\perp$ dependence of $e^{-3.2 p_\perp}$. The rapidity (y) and azimuthal angle (ϕ) distributions of these events were flat in the ranges $|y| < 0.5$ and $|\phi| < 40°$. Those events which satisfied the calorimeter trigger requirements were analyzed with the same software as the real events. Only those jets which were analyzed to have $|y| < 0.2$ and $|\phi| < 20°$ were used in the cross-section calculation, to help insure containment of the jet in the calorimeter. The acceptance was defined to be the ratio of the number of events analyzed to have a given $p_\perp$ and pass y and ϕ fiducial cuts, to the number of events generated at that $p_\perp$ within the fiducial range. This jet acceptance, including both geometrical and trigger contributions, is 95% for jet $p_\perp$'s well above trigger bias. This is partially by construction; the 40° cone size was selected to roughly balance the loss of trigger jet particles with the gain of background particles. We note, however, that if we simply used the calorimeter region (see fig. 16) as the jet definition region, the acceptance would be 70%. For the 200 GeV beam, there were seven sets of data: six different calorimeter biases, plus the interacting beam trigger. This enabled us to measure the jet cross section over a range of more than nine orders of magnitude. The overlapping (in $p_\perp$) of the data from different biases served as a check of the acceptance corrections. The acceptance corrected cross section for

$$pp \rightarrow jet + X$$

is shown in fig. 26 along with the QCD predictions. The upper curve is the cross section for producing a quark or gluon jet of given energy. The bottom curve is the cross section for producing a jet of given $p_\perp$. There is a factor of fifteen difference in cross sections in the two QCD curves. This rather large difference is due to energy appearing as particle masses, and transverse momentum of these particles about the jet axis (quark or gluon direction). It is proper to compare our data to the lower curve, for we have measured jets of specified $p_\perp$. The QCD prediction is about a factor of three lower than the data. This comparison is made without any adjustment to the model; note, for instance, the sensitivity of the cross section to parton internal transverse momentum (fig. 12). The QCD model was able to predict the observed $p_\perp$ dependence, $e^{-3.2 p_\perp}$. Also shown in fig. 26 are data on single particle production, $\frac{1}{2}(\pi^+ + \pi^-)$, from the Chicago-Princeton collaboration [27]. The jet to single particle ratio increases rapidly with increasing $p_\perp$, becoming $\simeq 700$ at $p_\perp = 6$ GeV/c.

A detailed acceptance calculation has been performed for the smaller sample of 130 GeV/c beam data in precisely the same manner as was done for the 200 GeV/c data. With the same jet definition the acceptance at 130 GeV/c is 32% lower than the acceptance at 200 GeV/c. This acceptance difference is due mainly to the smaller solid angle subtended by the calorimeters in the center of mass system for the 130 GeV/c data. The acceptance corrected invariant cross section
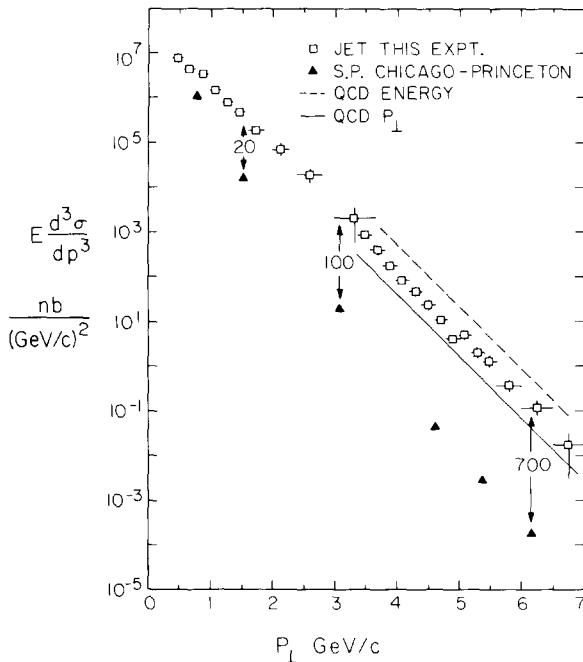
Fig. 26. The invariant cross section (squares) for pp→jet + X for 200 GeV incident protons. The lines are the QCD predictions (see text). The triangles are single particle data $\frac{1}{2}(\pi^+ + \pi^-)$ from ref. [27]; the numbers indicate the jet to single particle cross-section ratio.

for

$$pp \rightarrow jet + X$$
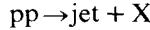
with 130 GeV/c incident protons is shown in fig. 27.

By measuring the cross sections at two c.m. energies ($\sqrt{s}$), it is possible to extract the $p_\perp$ dependence of the cross sections. We parameterize the invariant cross section as

$$E\frac{d^3\sigma}{dp^3} = \frac{f(x_\perp)}{p_\perp^n}$$

where $x_\perp \equiv 2p_\perp/\sqrt{s}$. If this parameterization holds true, then the ratio of jet cross sections at two different c.m. energies, but the same $x_\perp$, should be independent of $x_\perp$. The magnitude of this ratio determines n. Fig. 28 shows a plot of the ratio of invariant cross sections

$$\sigma_{(130\ \text{GeV})}/\sigma_{(200\ \text{GeV})} .$$

The ratio is plotted versus $x_\perp$. While the data do not rule out possible variation of
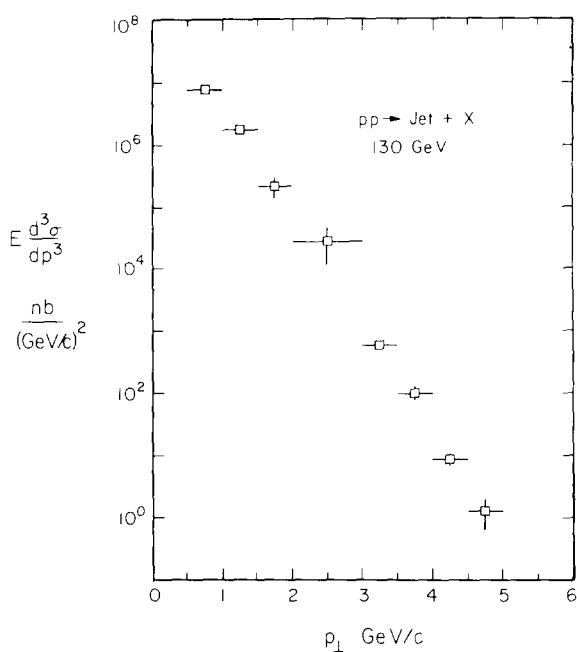
Fig. 27. Invariant cross section for pp→jet + X for 130 GeV incident protons.

this ratio with $x_\perp$, the data are consistent with no $x_\perp$ dependence. A fit gives $n = 6.3 \pm 0.3$ for the $p_\perp$ dependence of the cross section, using all the $x_\perp$ points. Jets at the smallest values of $x_\perp$ are likely to be dominated by single particles. At low $p_\perp$ ($p_\perp \leqslant 1.5$ GeV/c), the single particle cross section may be parameterized as $e^{-6p_\perp}$ or $e^{-3x_\perp\sqrt{s}}$ [1]. Our two lowest values of $x_\perp$ in fig. 28 are consistent with
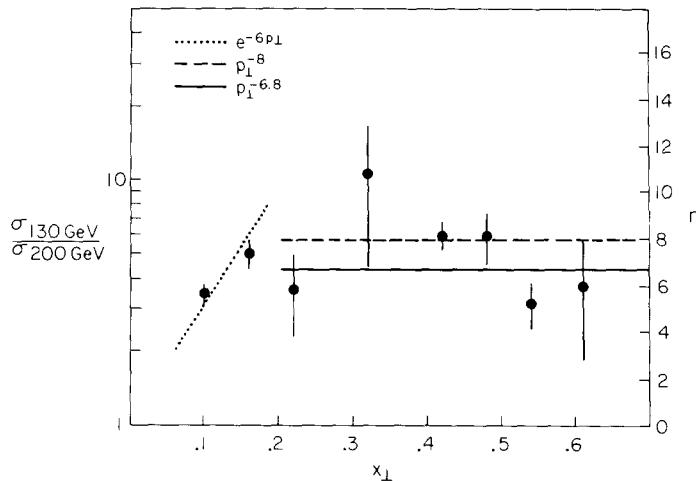
Fig. 28. The ratio of jet cross sections at 130 GeV to 200 GeV versus $x_\perp$. The right-hand vertical scale indicates the observed $p_\perp$ dependence (see text).
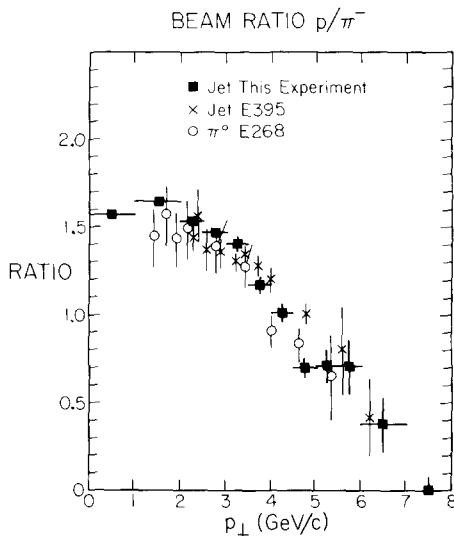
Fig. 29. The ratio of cross sections $\sigma_{(pp\rightarrow jet+X)}/\sigma_{(\pi^-p\rightarrow jet+X)}$ compared to the ratio $\sigma_{(pp\rightarrow jet+X)}/\sigma_{(\pi^+p\rightarrow jet+X)}$ from ref. [28] (crosses) and the ratio $\sigma_{(pp\rightarrow\pi^0+X)}/\sigma_{(\pi^-p\rightarrow\pi^0+X)}$ from ref. [29] (open circles). The $\pi^0 p_\perp$ has been divided by 0.8 (see text).

this. We consider this to be evidence against any large systematic error in the cross-section ratios of fig. 28. Another fit was done excluding the first two $x_\perp$ points and yielded $n = 6.8 \pm 0.4$. This is significantly flatter than the $p_\perp^{-8}$ dependence observed for single particle cross sections [27]. The different $p_\perp$ dependence for jets and single particles is predicted by QCD [7].

The rest of this section is concerned with jet production by different beam types. Fig. 29 shows the jet cross-section ratio:

$$\sigma_{(pp\rightarrow jet+X)}/\sigma_{(\pi^-p\rightarrow jet+X)} .$$

This ratio is roughly equal to the ratio of pp and π^-p total cross sections at low $p_\perp$, and decreases with increasing $p_\perp$. This is understood as being due to the fact that there is one less valence quark in the pion than in the proton. A single quark in the pion carries a greater fraction of the beam momentum, on the average, than does a single quark in the proton. There is, therefore, more energy available in the parton-parton c.m.s. on the average in πp interactions than in pp, so pions are able to make jets more easily at high $p_\perp$. Also shown are jet data from ref. [28]. Single-particle data from ref. [29] are given also, with the $p_\perp$ divided by 0.8. As noted previously, the single-particle data agree with the jet data when so plotted. This may be understood to be due to high-$p_\perp$ single particles arising from partons which had, on the average, 15–20% greater momentum [2, 5]. Fig. 30 shows this data as a function of $x_\perp$, along with the smaller sample of 130 GeV data. We observe a beautiful scaling with $x_\perp$.
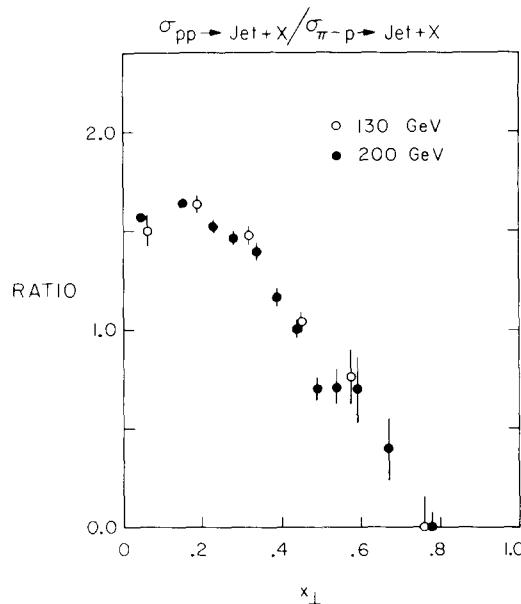
Fig. 30. The ratio of cross sections $\sigma_{(pp \to jet + X)}/\sigma_{(\pi^- p \to jet + X)}$ as a function of $x_\perp$ for 130 GeV beams (open circles) and 200 GeV beams (solid circles).

Two of the highest $p_\perp$ π^- induced jets are pictured in fig. 31. The momentum axes are defined in the $\pi^- p$ c.m.s., with the positive z direction corresponding to the beam direction. The electric charges of detected particles are labeled. Neutral particles are detected only in the calorimeter regions which are centered on the positive and negative x-axis of fig. 31. The jet $p_\perp$'s in these events correspond to nearly 80% of the kinematic limit.

Fig. 32 shows the jet cross-section ratio

$$\sigma_{(\pi^+ p \to jet + X)}/\sigma_{(\pi^- p \to jet + X)} \ .$$

Also shown are the single-particle data (also from this experiment),

$$\sigma_{(\pi^+ p \to h + X)}/\sigma_{(\pi^- p \to h + X)} \ ,$$

where h is any charged hadron. The single-particle $p_\perp$ scale is again divided by 0.8. Fig. 33 compares jet production by kaons and pions. We plot the ratios

$$\sigma_{(K^- p \to jet + X)}/\sigma_{(\pi^- p \to jet + X)} \ ,$$

$$\sigma_{(K^+ p \to jet + X)}/\sigma_{(\pi^+ p \to jet + X)} \ .$$
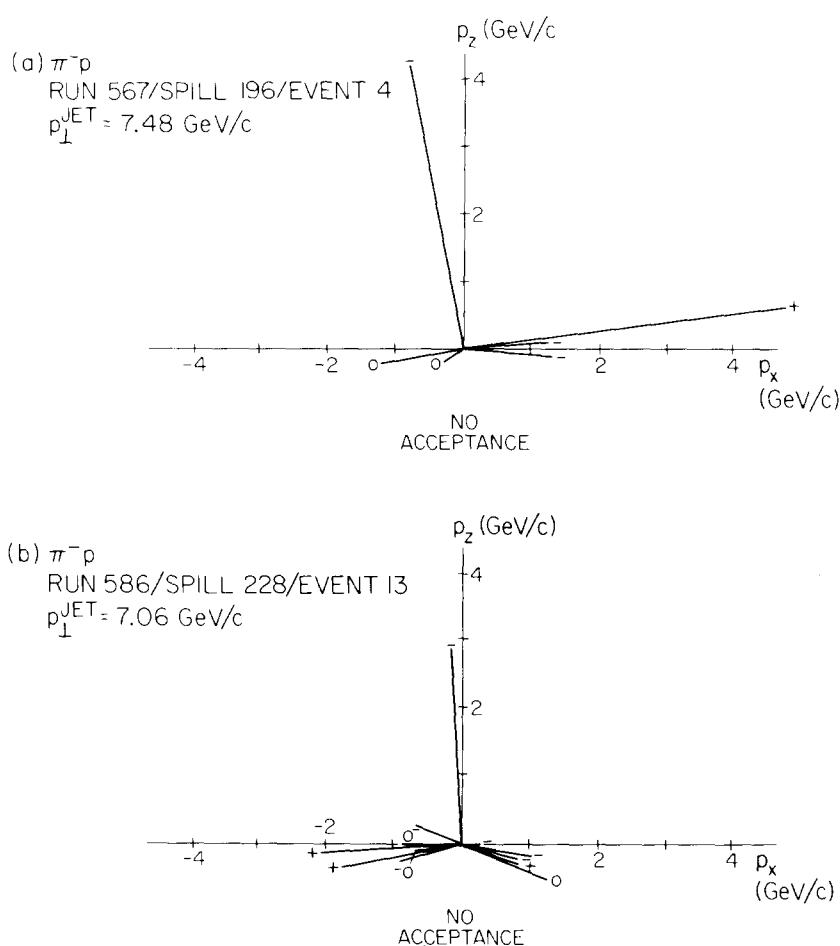
Fig. 31. Event pictures (in the c.m.s.) indicating the location of observed particles with their charge labeled for two of the highest $p_\perp$ jets observed.

The cross sections for jets induced by pions and kaons are equal (within statistical error) at high $p_\perp$. Fig. 34 compares jet production by protons and antiprotons. No significant $p_\perp$ dependence is seen in the ratio:

$$\sigma_{(pp \rightarrow jet + X)} / \sigma_{(\bar{p}p \rightarrow jet + X)} \;.$$

Also shown are single-particle data (π^0) from ref. [29].

Tables of all the jet cross sections measured in this experiment may be found in ref. [30].
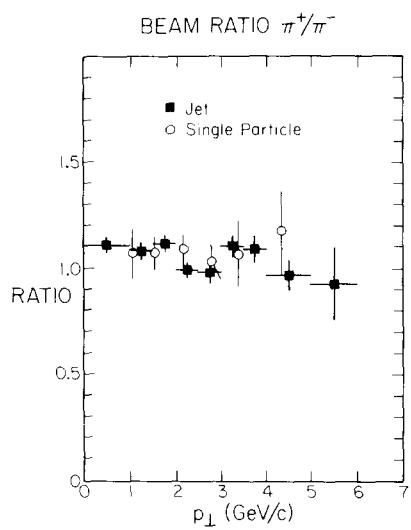
Fig. 32. The ratio of cross sections $\sigma_{(\pi^+ p \to jet + X)}/\sigma_{(\pi^- p \to jet + X)}$ compared with single-particle data ($p_\perp$ divided by 0.8).
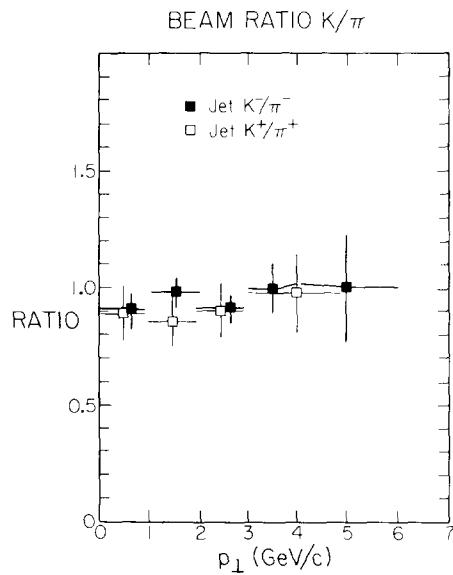

Fig. 33. The cross-section ratios $\sigma_{(K^- p \to jet + X)}/\sigma_{(\pi^- p \to jet + X)}$ and $\sigma_{(K^+ p \to jet + X)}/\sigma_{(\pi^+ p \to jet + X)}$.
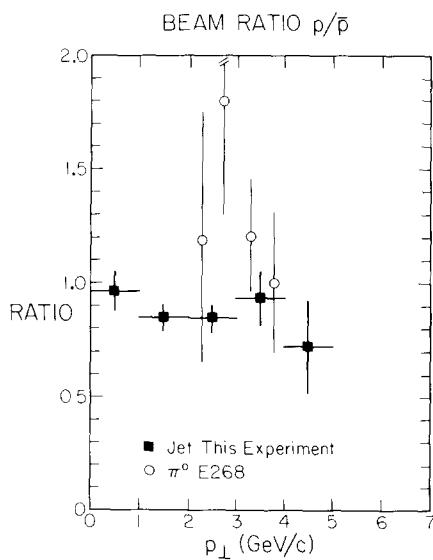
Fig. 34. The ratio of cross sections $\sigma_{(pp \to jet + X)}/\sigma_{(\bar{p}p \to jet + X)}$ compared with single-particle data (π^0) from ref. [29]. The $\pi^0 p_\perp$ has been divided by 0.8.

8. Conclusions

We have performed detailed Monte Carlo calculations as an essential step in understanding our high-$p_\perp$ jet data. This applies to both the jet cross-section measurements and the event structure. We have measured the invariant cross section for pp $\to$ jet + X for values of jet $p_\perp$ up to 7 GeV/c. The jet to single particle ratio increases dramatically with increasing $p_\perp$, becoming several hundred at high $p_\perp$. Jet cross sections for p, π^-, π^+, K^-, K^+, and $\bar{p}$ incident on a hydrogen target depend strongly on the number of valence quarks in the beam; those with two valence quarks make jets more easily at high $p_\perp$ than those with three quarks. By measuring the jet cross section at two c.m. energies, we were able to make a determination of the power behavior of the $p_\perp$ dependence. Parameterizing the jet cross section as $f(x_\perp)/p_\perp^n$ gives $n = 6.8 \pm 0.4$ (excluding low $x_\perp$ points).

A simple QCD picture was investigated where the events were idealized as a four-jet final state, arising from quark and gluon two-body scatters. The four-jet model does remarkably well in predicting both the large jet cross section and the event structure, without any "tuning" to the data. However, the fragmentation observed for the highest $p_\perp$ jets is softer than the QCD prediction from ref. [7]. Evidence has been presented for scale breaking in hadronic interactions. Such an effect is predicted by QCD, but the theory is not yet far enough advanced to make quantitative tests.

The positive to negative charge ratio of secondary hadrons is seen to decrease with increasing $|z|$ on both the trigger and away sides for both pp and $\pi^+ p$ jet

events. This ratio is roughly flat on both the trigger and away sides for $\pi^- p$ jet events. These ratios are understood theoretically, except for the $\pi^- p$ away side, in which the theory predicts too many negatives at high $|z|$.

Pion beams are seen to produce more high-$p_\perp$ particles on the away side at forward angles than a proton beam. The charge composition of these high-$p_\perp$ away side particles does not depend strongly on c.m. angle.

References

[1] M. Jacob and P.V. Landshoff, Phys. Reports 48 (1978) 285
[2] C. Bromberg et al., Phys. Rev. Lett. 38 (1977) 1447; Nucl. Phys. B134 (1978) 189; Proc. 8th Int. Symp. on Multiparticle dynamics, Kaysersberg, France, 1977, ed. R. Arnold, J.B. Gerber and P. Schübelin (Centre National de la Recherche Scientifique, Strasbourg, France, 1977)
[3] J. Rohlf, Ph.D. thesis, Caltech
[4] C. Bromberg et al., Phys. Rev. Lett. 42 (1979) 1202; 43 (1979) 561; 565
[5] G.C. Fox, Particles and fields, 1977, ed. G.H. Thomas, A.B. Wicklund, and P. Schreiner (American Institute of Physics, New York, 1978)
[6] M. Della Negra et al., Nucl. Phys. B127 (1977) 1
[7] R.P. Feynman, R.D. Field and G.C. Fox, Phys. Rev. D18 (1978) 3320
[8] G.R. Beausoleil and J. Rohlf, Caltech Memo CIT-64-79, unpublished;
    E. Malamud, unpublished
[9] E.B. Hughes et al., Nucl. Instr. 75 (1969) 130
[10] K. Yung, Ph.D. thesis, Caltech
[11] G.C. Fox, Caltech Memo CIT-14-75, unpublished
[12] K. Yung, Caltech Memo CIT-30-76, unpublished
[13] H. Georgi and H.D. Politzer, Phys. Rev. D14 (1976) 1829
[14] G.C. Fox, Nucl. Phys. B131 (1977) 107
[15] A.J. Buras, E.G. Floratos, D.A. Ross and G.T. Sachrajda, Nucl. Phys. B131 (1977) 308;
    A.J. Buras and K.J. Gaemers, Nucl. Phys. B132 (1978) 249
[16] H.L. Anderson, H.S. Matis and L.C. Myrianthopoulos, Phys. Rev. Lett. 40 (1978) 1061
[17] D.C. Hom et al., Phys. Rev. Lett. 36 (1976) 1239; 37 (1976) 1374;
    S.W. Herb et al., Phys. Rev. Lett. 39 (1977) 252;
    W.R. Innes et al., Phys. Rev. Lett. 39 (1977) 1240
[18] R. Cutler and D. Sivers, Phys. Rev. D16 (1977) 679; D17 (1978) 196
[19] B.L. Combridge, J. Kripfganz and J. Ranft, Phys. Lett. 70B (1977) 234
[20] R.D. Field and R.P. Feynman, Nucl. Phys. B136 (1978) 1
[21] R.P. Feynman, Proc. 8th Int. Symp. on Multiparticle dynamics, Kaysersberg, France (1977)
[22] R.D. Field, private communication
[23] J. Dakin et al., Phys. Rev. D10 (1974) 1401
[24] G. Hanson et al., Phys. Rev. Lett. 35 (1975) 1609
[25] F.W. Büsser et al., Nucl. Phys. B106 (1976) 1
[26] C. Bromberg et al., Nucl. Phys. B171 (1980) 38
[27] D. Antreasyan et al., Phys. Rev. Lett. 38 (1977) 112; Phys. Rev. D19 (1979) 764
[28] M.D. Corcoran et al., Phys. Rev. Lett. 41 (1978) 9
[29] G. Donaldson et al., Phys. Rev. Lett. 36 (1976) 110; 40 (1978) 917
[30] J. Rohlf, Caltech Memo CIT-65-79, unpublished, available from G.C. Fox, Caltech